JAAS

PAPER

View Article Online
View Journal | View Issue

Open Access Article. Published on 20 júní 2025. Downloaded on 2.11.2025 10:21:29.
This article is licensed under a Creative Commons Attribution-NonCommercial 3.0 Unported Licence.

Check for updates

Cite this: *J. Anal. At. Spectrom.*, 2025, **40**, 2408

Evaluation of laser-induced and ICP-induced elemental fractionation using laser ablation-ICP-TOFMS†

D. Käser, [a] T. Van Acker, [b] J. Koch, [a] B. Hattendorf [a] and D. Günther *[a]

The composition of laser-generated aerosols produced during single spot ablation was analyzed *via* inductively coupled plasma time-of-flight mass spectrometry (LA-ICP-TOFMS) and compared with that of the same material deposited on the sample surface. Differences between the signals recorded from single spot ablation and the subsequent deposit analysis enabled studying and exploring non-stoichiometric processes at the ablation site. These measurements allowed for the determination of the transport efficiencies of the elements present in NIST SRM 610, which were element-specific and always higher than 85%. A mass balance of $^{238}U^+/^{232}Th^+$ signal intensity ratios allowed the differentiation of laser-induced and ICP-induced elemental fractionation using only LA-ICP-TOFMS data, without the need for the off-line analysis of the collected material. All phenomena reported herein were studied using a range of parameters for single spot ablation including different laser fluences (7.4–25 J cm^{-2}) and number of pulses per spot (100–600 pulses). The method presented here provides direct access to important parameters that influence the accuracy of quantitative analysis using LA-ICPMS, such as the amount and composition of the deposited material around the crater and information about the aforementioned transport efficiencies of individual elements. In addition, the proposed analysis and calculation procedure allowed to distinguish between laser- and ICP-induced elemental fractionations for different LA and ICPMS operating conditions. Knowledge about these parameters will help understand the ablation behavior of different matrices and may therefore improve non-matrix matched quantification using LA-ICPMS.

Received 29th April 2025
Accepted 19th June 2025

DOI: 10.1039/d5ja00173k

rsc.li/jaas

Introduction

The combination of laser ablation (LA) with inductively coupled plasma mass spectrometry (ICPMS) has been rapidly accepted as a new method for direct solid sample analysis with high spatial resolution.[1] The evaluation of LA-ICPMS for geological applications, such as for the determination of rare-earth elements in various minerals[2] and U–Pb isotopic analysis for the age determination of zircons,[3] has demonstrated the capabilities of the method. However, inter-element fractionation has been a major limitation. Fryer *et al.*[4] defined elemental fractionation as the temporal change in an element's signal intensity ratios relative to Ca during single spot ablation. Their "fractionation indices" represent the signal intensity ratios of the second half of a transient signal divided by the first half of the signal over 4 minutes. This calculation procedure has also been used over time to demonstrate improvements achievable with new instrument developments.[5] Fractionation effects were particularly reduced using nanosecond (ns) lasers with wavelengths below 200 nm,[6,7] or a shorter pulse length in the femtosecond (fs) range.[8] The reduction in fractionation effects was confirmed by comparing ns and fs laser ablation for craters generated with 2400 pulses of single spot ablation. Values obtained by fs-LA indicated lower signal variation over time; however, elemental fractionation was still visible.[5]

While fractionation effects were shown to be reduced by improving the laser ablation systems used, non-stoichiometric detection and analysis still remained a challenge, with fractionation indices deviating from 1 for various elements.[4,5] These studies indicated that the fractionation index describes processes affecting the detection of element intensity ratios and heavily depends on operating conditions. For example, a comparison of fractionation indices for different crater aspect ratios (*i.e.* depth-to-diameter ratio) and by varying the ablation rates of individual laser ablation systems showed highly variable fractionation effects.[9]

Another indicator that has been proposed for instrument optimization is the $^{238}U^+/^{232}Th^+$ signal intensity ratio, which

[a]*Laboratory of Inorganic Chemistry, Department of Chemistry and Applied Biosciences, ETH Zürich, Vladimir-Prelog-Weg 1, 8093 Zurich, Switzerland. E-mail: guenther@inorg.chem.ethz.ch*

[b]*Atomic and Mass Spectrometry Research Unit (A&MS), Department of Chemistry, Ghent University, Krijgslaan 281-S12, 9000 Ghent, Belgium*

† Electronic supplementary information (ESI) available. See DOI: https://doi.org/10.1039/d5ja00173k

 This journal is © The Royal Society of Chemistry 2025

Open Access Article. Published on 20 júní 2025. Downloaded on 2.11.2025 10:21:29.
This article is licensed under a Creative Commons Attribution-NonCommercial 3.0 Unported Licence.

must be close to one for the NIST SRM 610 glass standard.[10] This is because both elements are present in a very similar concentration in the reference material and have almost equal ionization energies and only a small mass difference. Sensitivity ratios higher than one can be attributed to incomplete aerosol vaporization, which also affects elemental fractionation in LA-ICPMS.[11] Incomplete vaporization, atomization and ionization of laser-generated particles are considered less severe for ablation in helium with 193 nm LA in comparison with 266 nm in argon.[12] Using the latter, it has been shown that 150 nm is a critical size, above which the laser-generated aerosol particles of NIST SRM 610 show incomplete ionization.[13] The previously observed decrease in fractionation effects while using a nanosecond 193 nm laser was then related to smaller particles and narrower particle size distribution of the aerosol generated.[14] A better understanding of the conditions affecting these fractionation effects has helped establish the use of shorter wavelength lasers[15] and minimize ICP-induced fractionation by adjusting the $^{238}U^{+}/^{232}Th^{+}$ signal intensity ratio to their concentration ratio.[10]

Minimizing elemental fractionation is key to applications such as U–Pb geochronology, where elemental fractionation limits the precision and accuracy of mineral dating.[15] For these studies, specific attention must be paid to the sensitivity ratios of U/Th and Pb/U.[16] In this context, the aspect ratio of the crater affects the signal of uranium, whereas, lead undergoes constant material loss, independent of the crater size.[17] Material losses on the sample surface also lead to non-stoichiometric composition with variations in the Pb/U and Pb/Th ratios of the deposits surrounding the ablation craters.[16] This is in general agreement with the preliminary analyses of the surface condensate reported by Eggins *et al.*,[7] demonstrating an enrichment in volatile elements compared to more refractory ones.

ICP-related fractionation effects have, however, never been clearly distinguished from laser-induced fractionation. It has been shown that the aerosol produced by the laser ablation of brass differs in composition from the bulk material.[18] Together with the fact that the composition of the deposited material also differs from the bulk composition of the analyzed samples,[7,16] this implies that elemental fractionation occurs even during the sampling process. In order to distinguish ICP-related and laser-ablation-dependent elemental fractionation, a better understanding of fractionation that occurs during laser ablation sampling is necessary. By analyzing the composition of the aerosol generated during single spot ablation and the deposited material under identical ICPMS operating conditions, the degree of fractionation at the ablation site can be evaluated.

This study thus employs single spot ablation of the NIST SRM 610 glass standard, followed by re-ablation of the entire deposit around the crater, based on a low-fluence sampling approach ($\leq$1 J cm^{-2}). Signals monitored during single spot ablation and the ablation of the deposits were recorded under identical ICPMS operating conditions. This approach enabled mass balance calculations to determine individual transport efficiencies of all monitored isotopes. By using ICP-TOFMS, the signal intensity ratios of the isotopes of interest could be monitored quasi-simultaneously, allowing a comprehensive description of the composition and spatial distribution of the deposits. These experiments were carried out under various ablation conditions and by varying the laser fluence, number of pulses and crater diameter to investigate their impact on the amount and composition of the individual materials transported and deposited during laser ablation.

Using this experimental setup, we were able to show that laser-induced fractionation reproduces the pattern of fractionation indices published by Fryer in 1995.[4] The Laser-Induced Fractionation Indices (LIFI) introduced here indicate that even though the fractionation effects can be reduced significantly, they are associated with laser–matter interactions. The results allow us to distinguish laser-induced and ICP-induced fractionations. Both sources of fractionation can be isolated based on the relative element abundance determined in the deposits and the initial spot.

Experimental details

Instrumentation

A homogenized laser beam generated by an argon-fluoride (ArF) excimer laser system (193 nm, GeoLas C, Lambda Physik, Germany) was used to ablate the samples placed in an in-house developed modified parallel-flow ablation cell (MPFAC).[19] This low-dispersion ablation cell provided short washout times (<200 ms) even for larger spot sizes, which enabled signal monitoring during single spot ablation, as well as mapping the spatial distribution of the deposits surrounding the crater. Similar to the study that first described this ablation cell design,[20] ablation was carried out in helium (99.999%, Linde Gas Schweiz AG, Switzerland), and argon (99.999%, Linde Gas Schweiz AG, Switzerland) was added above the ablation site. The ion signals were acquired using an ICP-TOFMS instrument (icpTOF 2R, TOFWERK AG, Switzerland). Daily optimization of the operating conditions was carried out by maximizing the signal intensity of $^{238}U^{+}$ while maintaining a $^{238}U^{+}/^{232}Th^{+}$ signal intensity ratio close to 1 during the ablation of a NIST SRM 610 glass standard. The optimization aimed to achieve complete vaporization and atomization of the sample and was performed by ablating a line scan known to produce a greater fraction of larger aerosol particles (Table 1).[11]

The mass fractions and isotope abundance values used in the data evaluation of NIST SRM 610 were obtained from the GeoReM Database.[21,22]

Signal evaluation

All data processing steps were performed using in-house-written R-scripts in the RStudio environment.[23,24] For single spot ablation experiments, the background signal was recorded for 45 s without laser firing, followed by the transient ablation signal. Ablation was carried out on a freshly polished surface wiped with isopropanol. The background signals in all experiments were corrected for drift by linear interpolation of the signals recorded at the beginning of the subsequent measurements. The ion signals recorded during single spot ablation

Open Access Article. Published on 20 júní 2025. Downloaded on 2.11.2025 10:21:29.
This article is licensed under a Creative Commons Attribution-NonCommercial 3.0 Unported Licence.

Table 1 Summary of the operating conditions of the laser and ICPMS used for single spot ablation and deposit analysis (imaging)

Laser ablation			ICP-TOFMS	
	Spot ablation	Imaging		
Repetition rate	10 Hz	5 Hz	Make-up gas flow rate (Ar)	0.7–0.8 L min^{-1}
Spot size	24–44 μm	32 μm	Carrier gas flow rate (He)	1.3–1.4 L min^{-1}
Step size	—	10 μm	Sampling depth	3.2–4.5 mm
Fluence	7.4–25 J cm^{-2}	≤1 J cm^{-2}		
			Plasma power	1550 W
Image size			Auxiliary gas flow rate	0.8 L min^{-1}
Raster size/μm	1000 × 1000 (44 μm craters)		Plasma gas flow rate	16 L min^{-1}
	500 × 500 (24 μm craters)			

were summed for the entire ablation period. Sensitivity drift was also corrected by linear interpolation of the signals of NIST SRM 610 measured using a raster scan (20 × 20 spots, 1 laser pulse/spot) at the start and the end of each sequence. For the deposits (Fig. 1), the fluence was lowered to 1 J cm^{-2} (low-fluence imaging) to reduce the signal contribution from co-ablation, *i.e.* mass removal of the pristine glass substrate material below the deposits. Lower fluences were tested but were found to be insufficient to remove the deposited material entirely. Instead of re-mobilizing, the deposit appeared to melt on the sample surface and could not be removed by mechanical wiping.

The area considered for signal integration from the deposits was adjusted to a region of interest (ROI) where the deposition was visible using light microscopy. The signals recorded for each line scan were corrected for co-ablation using the average value obtained from the same line upstream of the carrier gas flow in the ROI to avoid potential contributions from deposits caused by gas dynamics. Despite the use of a lower fluence in the imaging experiments, co-ablation occurred especially for the more volatile elements in NIST SRM 610 (*e.g.* Pb). In particular, in experiments with a low amount of deposited material (low pulse number and fluence), the correction required for co-ablation can thus be substantial and may affect the results.

Theoretical considerations

The approach proposed here for the characterization of laser-induced fractionation relies on a set of assumptions. One basic assumption is that the number (N) of isotopes (i) present in the aerosol generated from single spot ablation ($N(i)_A$) plus the isotopes deposited on the sample surface ($N(i)_D$) corresponds to the total number of isotopes present in the ablated volume ($N(i)_{tot}$).

$$N(i)_A + N(i)_D = N(i)_{tot} \quad (1)$$

This assumption also implies negligible transport losses in comparison with the deposit losses, which was already suggested when helium was initially introduced as ablation environment.[7] Transport losses in the tubing between the LA cell and the ICP unit were also considered insignificant because aerosol throughput is independent of tubing length.[25] In addition, no significant differences in transport efficiency have been reported between different cell designs. Therefore, we did not consider further losses in the ablation cell and its fittings to the tubing.[26] Nevertheless, the ablation cell used in this study was optimized to minimize aerosol dispersion using high velocity but still laminar gas flows,[20] making substantial losses downstream of the ablation site highly unlikely. Similarly, the material losses on the crater walls are not considered as these

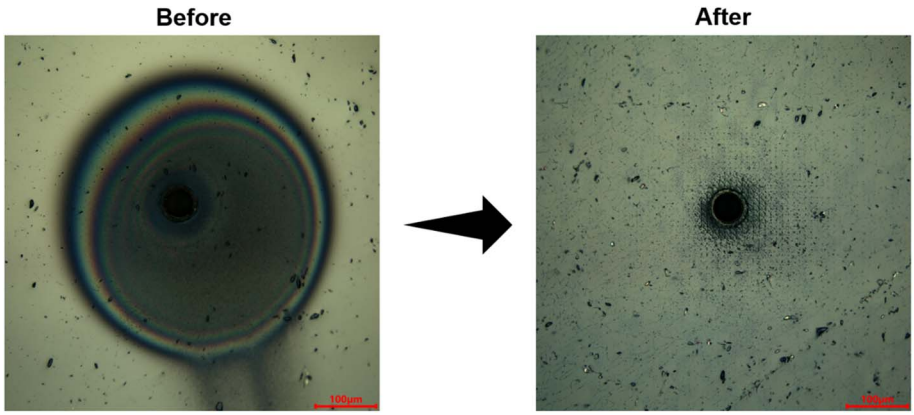

Fig. 1 Light microscopy images of 600-pulses craters of 44 μm diameter formed in helium using a fluence of 20 J cm^{-2} before (left) and after (right) deposit removal. With low-fluence imaging analysis, a limited amount of material can still be observed in the vicinity of the crater, but no substantial modification of the sample surface was observed.

Open Access Article. Published on 20 júní 2025. Downloaded on 2.11.2025 10:21:29.
This article is licensed under a Creative Commons Attribution-NonCommercial 3.0 Unported Licence.

particles are observed only on the upper part of craters with extreme depth-to-diameter ratios.[9]

Another assumption is that the material removed from the crater represents the exact composition of the sample, *i.e.*, stoichiometric, which allows the expansion of eqn (1) to isotope number ratios, as presented in eqn (2), for isotopes x and y in relation to their concentration (c) ratio.

$$\frac{N(x)_{\mathrm{A}} + N(x)_{\mathrm{D}}}{N(y)_{\mathrm{A}} + N(y)_{\mathrm{D}}} = \frac{N(x)_{\mathrm{tot}}}{N(y)_{\mathrm{tot}}} = \frac{c(x)}{c(y)} \tag{2}$$

The respective number of atoms, however, cannot be detected directly because the element-specific ion yields[27] and mass-dependent transmission[28] manifest in the ICPMS mass spectra. The number of ions (I) detected is thus always lower than the number of atoms delivered to the ICP. This is accounted for by introducing the isotope-specific factor P, as shown in eqn (3):

$$N(i) \times P(i) = I(i) \tag{3}$$

Assuming that factor $P(i)$ is equal for both single spot ablation and deposits analysis (under the same ICPMS conditions), these equations allow the estimation of the transport efficiency (TE(i)) for each isotope from the measured signals:

$$\mathrm{TE}(i) = \frac{N(i)_{\mathrm{A}}}{N(i)_{\mathrm{A}} + N(i)_{\mathrm{D}}} = \frac{P(i) \times I(i)_{\mathrm{A}}}{P(i) \times \left(I(i)_{\mathrm{A}} + I(i)_{\mathrm{D}}\right)} = \frac{I(i)_{\mathrm{A}}}{I(i)_{\mathrm{A}} + I(i)_{\mathrm{D}}} \tag{4}$$

Notably, the P factors cancel out since they are assumed identical for the single spot and deposit ablation experiments, and the temporal drift was corrected by bracketing. As the only losses considered here are for the deposits next to the ablation site, the relative portion of the material deposited for a given isotope can also be expressed as "deposit fraction" (DF(i)), which is defined similarly to the TE.

$$\mathrm{DF}(i) = \frac{N(i)_{\mathrm{D}}}{N(i)_{\mathrm{A}} + N(i)_{\mathrm{D}}} = \frac{I(i)_{\mathrm{D}}}{I(i)_{\mathrm{A}} + I(i)_{\mathrm{D}}} = 1 - \mathrm{TE}(i) \tag{5}$$

The laser-induced fractionation index (LIFI) then represents the relative degree of preferential deposition of the elements and can be defined as the ratio of DFs for any combination of isotopes x relative to a reference isotope y:

$$\mathrm{LIFI}(y) = \frac{N(x)_{\mathrm{D}}}{N(x)_{\mathrm{A}} + N(x)_{\mathrm{D}}} \times \frac{N(y)_{\mathrm{A}} + N(y)_{\mathrm{D}}}{N(y)_{\mathrm{D}}} = \frac{\mathrm{DF}(x)}{\mathrm{DF}(y)} \tag{6}$$

As shown by the equations above, element-specific sensitivity cannot be derived directly, but the relative factors can be calculated using eqn (1)–(3) for isotopes x and y, as shown in eqn (7).

$$\frac{P(x)}{P(y)} = \frac{I(x)_{\mathrm{A}} + I(x)_{\mathrm{D}}}{N(x)_{\mathrm{A}} + N(x)_{\mathrm{D}}} \times \frac{N(y)_{\mathrm{A}} + N(y)_{\mathrm{D}}}{I(y)_{\mathrm{A}} + I(y)_{\mathrm{D}}} = \frac{I(x)_{\mathrm{A}} + I(x)_{\mathrm{D}}}{I(y)_{\mathrm{A}} + I(y)_{\mathrm{D}}} \times \frac{c(y)}{c(x)} \tag{7}$$

This expression resembles the absolute sensitivity ratio for the isotopes as it includes the entire ablated material and not just the transported fraction.

Results and discussion

Impact of the laser fluence

To evaluate the effect of laser fluence on the degree of sample deposition and transport efficiency, craters of 44 μm diameter were ablated using laser fluences ranging from 7.4 to 25 J cm^{-2} by applying 600 pulses in total for each experiment. Single spot ablation was followed by sweeping the deposits from the sample surface using the low-fluence imaging approach across a square ROI of 1 mm^2 around the crater. Increasing the laser fluence led to larger areas of sample material deposition, which can be observed based on the $^{232}Th^+$ signal intensity maps displayed in Fig. 2. This observation agrees with the findings of Eggins *et al.*,[7] who reported that material deposition reduced at lower laser fluences.

Based on these maps, the signal intensities corrected for co-ablation were integrated across the respective ROIs to determine the deposited material fraction. As illustrated in Fig. 3, the $^{232}Th^+$ and $^{238}U^+$ signal intensities increased for both single spot and deposit ablation with increasing laser fluences. However, the deposit signals at fluences higher than 15 J cm^{-2} increased more steeply, while the slope of the signal from single spot ablation continuously decreased with increasing fluences.

Based on these data, the transport efficiencies of Pb, Th and U were calculated. As displayed in Fig. 4, the transport efficiencies of all elements decreased with increasing fluence and their losses increased with their volatility. The TEs calculated from these experiments were in the order Th > U > Pb, with values between 99% and 95% for Th, 99% and 93% for U and 95% to 90% for Pb.

As seen in Fig. 3, the change in signal intensity with increasing fluence was not equal for all investigated isotopes. While Th exhibited a relatively stronger increase than U during single spot ablation, its ion signals from the deposits were always lower. The corresponding intensity ratios $^{238}U^+/^{232}Th^+$ and $^{208}Pb^+/^{238}U^+$ are listed in Table 2. The variability was smaller for the single spot ablation experiments, but a decreasing trend of $^{238}U^+/^{232}Th^+$ signal intensity ratio was observed at higher fluence, while only a minute increase was observed for $^{208}Pb^+/^{238}U^+$. The ion signals from deposit ablation, however, indicated a substantial decrease in both ratios. The deposit signals revealed a trend towards the expected concentration ratios of the isotopes ($\approx$1.01 for $^{238}U^+/^{232}Th^+$ and $\approx$ 0.49 for $^{208}Pb^+/^{238}U^+$),[21,22] along with the depletion of the more volatile element with increasing fluence, as shown in Table 2. As for the single spot ablation experiments, on the other hand, there was no unique trend with respect to element volatility. While U/Th decreased continuously and reached a value below the concentration ratio of the isotopes, the Pb/U ratio remained almost stable (or rather appeared to increase) with fluence and was always higher than the concentration ratio in NIST SRM 610.

Open Access Article. Published on 20 juni 2025. Downloaded on 2.11.2025 10:21:29.
This article is licensed under a Creative Commons Attribution-NonCommercial 3.0 Unported Licence.

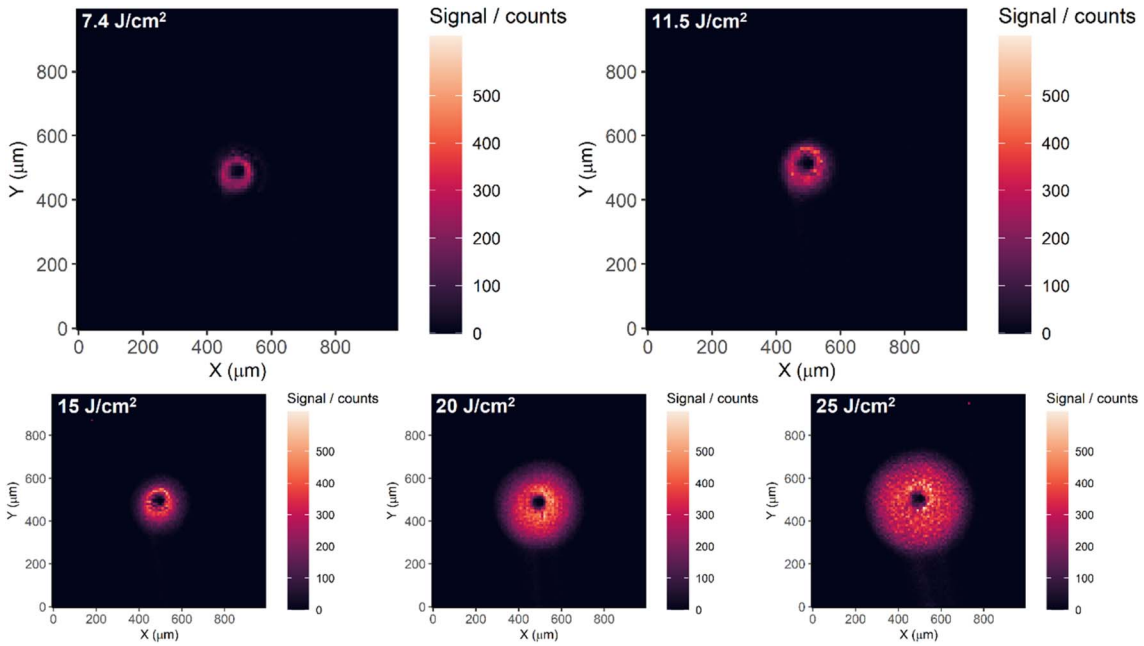

Fig. 2 $^{232}Th^{+}$ raw signal intensity maps of 600-pulses craters of 44 µm diameter ablated using different fluences.

Impact of the crater aspect ratio

In a second set of experiments, ion signals from single spot ablation and deposit imaging were recorded for LA with an increasing number of laser pulses (100–600 pulses) at the lowest fluence (7.4 J cm^{-2}). The deposits were again analyzed using the low-fluence imaging approach. As illustrated in Fig. 5, the ion signal intensities showed a similar trend to that of increasing fluence. The ion counts obtained from the single spot ablation experiments increased sub-proportional to the number of pulses applied, while the ion counts from the deposits increased almost linearly until 300 pulses. In particular, the $^{238}U^{+}$ ion signals increased less steeply above 300 pulses. In contrast to the experiments carried out with varying laser fluences, however, the change in the respective TEs (Fig. S1†) was substantially smaller, indicating a decrease in the overall ablated volume.

The signal intensity ratios (Table 3) in the 600-pulses experiment were generally comparable to the values obtained with 7.4 J cm^{-2} in the previous experiment (Table 2). However, the data generated with the same conditions

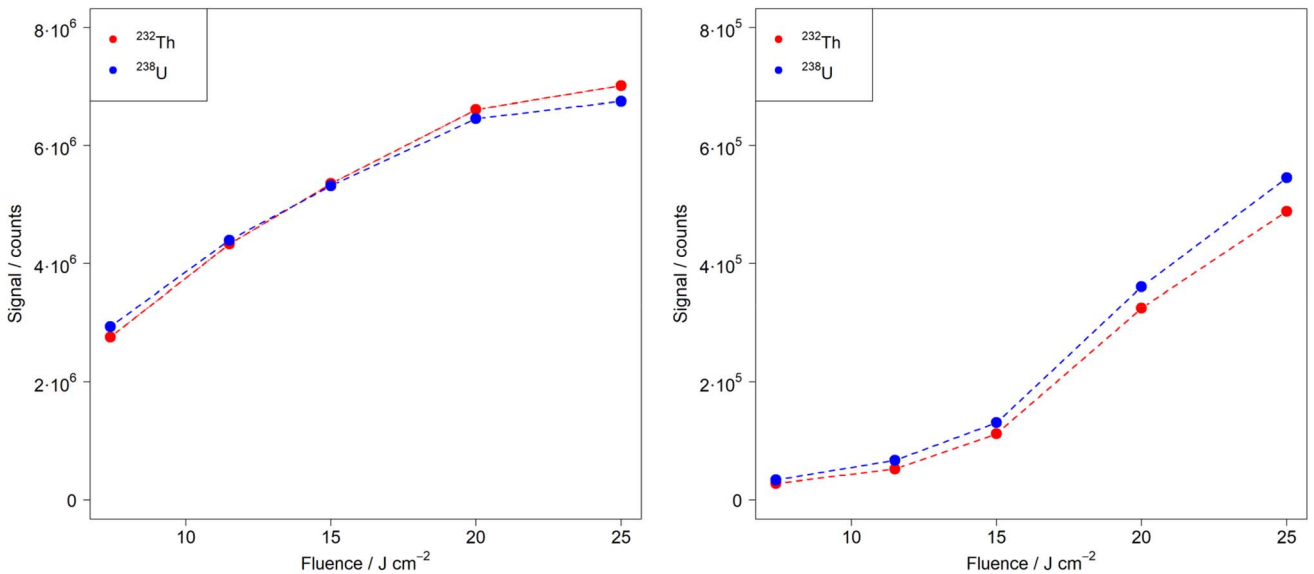

Fig. 3 $^{232}Th^{+}$ and $^{238}U^{+}$ signal intensities measured during 600-pulses single spot ablation at different fluences between 7.4 and 25 J cm^{-2} (left) and deposit removal near the corresponding craters (right).

Open Access Article. Published on 20 júní 2025. Downloaded on 2.11.2025 10:21:29.
This article is licensed under a Creative Commons Attribution-NonCommercial 3.0 Unported Licence.

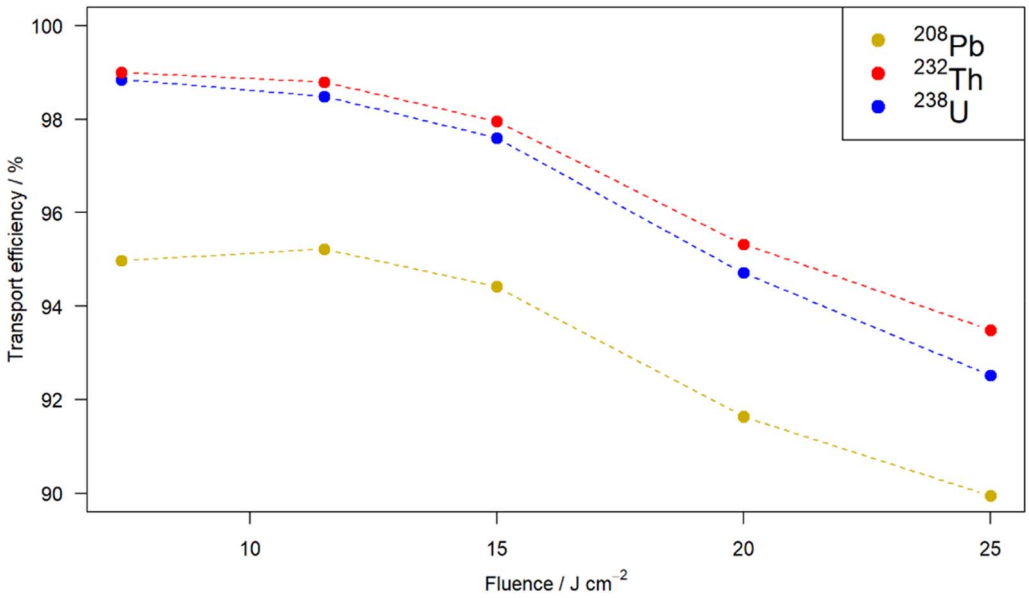

Fig. 4 Transport efficiencies obtained as a function of the fluence for $^{208}Pb^+$, $^{232}Th^+$ and $^{238}U^+$.

(600 pulses, 7.4 J cm^{-2}) differed between the experiments, highly likely because of the different operating conditions of the instrument, as the experiments were carried out on different days. During single spot ablation, the $^{238}U^+/^{232}Th^+$ signal intensity ratios were lower than the ones obtained in the fluence variation experiment and dropped to values below the concentration ratio. The $^{208}Pb^+/^{238}U^+$ signal intensity ratios, on the other hand, were higher than those observed in the fluence variation experiment and showed a steeper increase with the number of pulses. The intensity ratio, in this case, was also always higher than the concentration ratio. Moreover, the intensity ratios of $^{238}U^+/^{232}Th^+$ in the deposits were higher than the concentration ratio and dropped below this value as the number of pulses increased. The $^{208}Pb^+/^{238}U^+$ intensity ratio was always substantially higher than the concentration ratio of 0.49 and showed a decreasing trend when the number of pulses was increased beyond 200. At a lower number of laser pulses, we assume that the signals were affected to a greater extent by co-ablation correction and were, therefore, not considered.

To investigate the effect of the depth-to-diameter ratio of the crater in more detail, the same experiment was repeated for craters with a diameter of 24 μm (Table S1†). The intensity ratios obtained from single spot ablation were lower and less variable for $^{238}U^+/^{232}Th^+$, while the $^{208}Pb^+/^{238}U^+$ intensity ratios were more than 10% higher and increased notably with increasing crater depth. Notably, the signal intensity ratios were similar to those obtained for a crater diameter of 44 μm with twice the number of laser pulses, which would hence have a similar depth-to-diameter ratio. The ratios obtained from deposit analyses exhibited a greater scattering, which can be attributed to the comparably low amount of the deposited material. The enrichment of the more volatile element in the deposits, however, appeared to be more pronounced in this case.

Table 2 $^{208}Pb^+/^{238}U^+$ and $^{238}U^+/^{232}Th^+$ elemental ratios of the mean signals measured for single spot ablation and deposit analyses of a 44 μm diameter crater using 600 pulses with different fluences

	$^{238}U^+/^{232}Th^+$		$^{208}Pb^+/^{238}U^+$	
Fluence	Single spot ablation	Deposit removal	Single spot ablation	Deposit removal
7.4 J cm^{-2}	1.06	1.22	0.67	3.06
11.5 J cm^{-2}	1.02	1.28	0.67	2.20
15 J cm^{-2}	0.99	1.17	0.67	1.61
20 J cm^{-2}	0.98	1.11	0.68	1.10
25 J cm^{-2}	0.96	1.12	0.68	0.94

The $^{88}Sr^+/^{43}Ca^+$ and $^{139}La^+/^{140}Ce^+$ intensity ratios were also evaluated in detail (Table S2†), which indicated that Sr and Ca experienced very similar fractionation trends, only little variation between different crater aspect ratios and even between the single spot ablation and deposit analyses. The ratios, however, differed substantially from their concentration ratio because of the mass discrimination in ICP-TOFMS. The measured $^{139}La^+/^{140}Ce^+$ signal intensity ratios, alternatively, demonstrated the relative enrichment of Ce in both deposits and single spot ablation in comparison with the corresponding concentration ratio. The enrichment decreased in both cases as the aspect ratio of the crater increased and was more pronounced in the deposits, in general. These observations are consistent with the additional +4 oxidation state of Ce and its higher volatility compared to La.[29,30]

The three previous experiments indicate common trends in the measured intensity ratios of $^{238}U^+/^{232}Th^+$ and $^{208}Pb^+/^{238}U^+$ when the aspect ratio of the laser-generated crater increases, either using higher pulse energies for the same number of pulses or by applying more laser pulses of the same fluence. For $^{208}Pb^+/^{238}U^+$, this is in good agreement with all previous reports on elemental fractionation, that is, the intensity ratio obtained

Open Access Article. Published on 20 júní 2025. Downloaded on 2.11.2025 10:21:29.
This article is licensed under a Creative Commons Attribution-NonCommercial 3.0 Unported Licence.

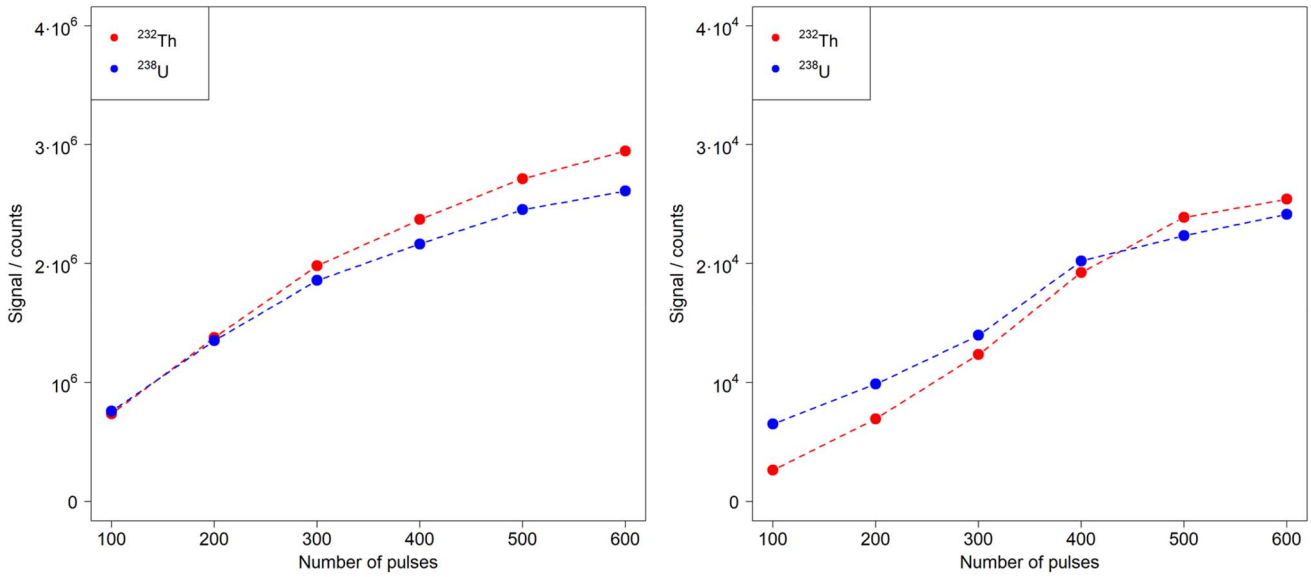

Fig. 5 $^{232}Th^+$ (red) and $^{238}U^+$ (blue) signals obtained during single spot ablation (left) and deposit removal (right) for craters of different depths formed using a fluence of 7.4 J cm^{-2} and a spot size of 44 μm diameter.

from single spot ablation generally increases with increasing crater aspect ratios.[16] The corresponding decrease observed for $^{238}U^+/^{232}Th^+$ also agrees with previous observations and can be attributed to a change in the particle size distribution, that is, a greater fraction of smaller particles are formed from deeper craters, as suggested by Kuhn *et al.*[14]

Notably, the measurements were carried out after optimizing the He carrier gas and Ar make-up gas flows in combination with the sampling depth to ensure a $^{238}U^+/^{232}Th^+$ sensitivity ratio near 1 for single pulse ablation, *i.e.* always ablating the pristine surface of a NIST SRM 610 glass standard, which led to a substantial fraction of large particles in the aerosol. This was done to ensure that particles of all sizes could be efficiently vaporized in the ICP. As the crater aspect ratio increased during the experiments, the particle size distribution during single spot ablation changed to smaller average sizes,[14] and the earlier vaporization of $^{238}U^+$ *vs.* $^{232}Th^+$ led to a stronger loss by diffusion within the ICP. At the same time, however, the deposits formed from craters with a higher aspect ratio were found to be increasingly depleted in U relative to Th even though they were all ablated from the sample surface directly, regardless of the crater aspect ratio. Yet, all $^{238}U^+/^{232}Th^+$ intensity ratios determined for deposits from craters with the lowest aspect ratio were substantially higher than the concentration ratio. This implies an enrichment of Th *vs.* U in the aerosol transported to the ICP from the ablation site during single spot ablation. Based on this reasoning, the measured $^{208}Pb^+/^{238}U^+$ intensity ratios imply that an even stronger enrichment of the more volatile element Pb occurred in the deposited material. While the intensity ratios recorded during single spot ablation were higher by 30–50% than the isotope concentration ratios in NIST SRM 610, as listed in Table 3, the deposits exhibited 8.5 to 9.5-fold higher values at low laser fluences, which decreased to approximately 2-fold at the highest fluence used.

Table 3 $^{238}U^+/^{232}Th^+$ and $^{208}Pb^+/^{238}U^+$ ratios measured for single spot ablation and deposit analysis of 44 μm craters formed using a fluence of 7.4 J cm^{-2}

	$^{238}U^+/^{232}Th^+$		$^{208}Pb^+/^{238}U^+$	
Crater depth	Single spot ablation	Deposit removal	Single spot ablation	Deposit removal
100 pulses	1.03	2.46	0.69	4.04
200 pulses	0.98	1.42	0.70	4.57
300 pulses	0.94	1.13	0.71	4.69
400 pulses	0.91	1.05	0.73	4.24
500 pulses	0.90	0.94	0.75	4.12
600 pulses	0.89	0.95	0.77	4.16

Laser-induced fractionation

The results from the previous experiments imply that two independent fractionation processes happen during LA-ICPMS analyses. The mass-balance-based Laser-Induced Fractionation Indices (LIFI in eqn (6)) were thus used to assess the magnitude of elemental fractionation occurring specifically at the ablation site. The LIFI were determined for a broad range of isotopes using $^{88}Sr^+$ as the reference isotope. This enabled a direct comparison with the fractionation indices defined by Fryer *et al.*[4] Instead of using Ca as the reference element, we opted for Sr because of its higher sensitivity in ICP-TOFMS and similar fractionation behavior (Table S2 and Fig. S2†). The LIFI obtained from experiments with increasing fluences and pulse numbers are displayed in Fig. 6. In all cases, distinctly higher values were observed for elements characterized by relatively low condensation temperatures.[29] The magnitude of the LIFI was, however, strongly affected by the laser ablation conditions used. They were found to be substantially close to 1 even for the

Open Access Article. Published on 20 júní 2025. Downloaded on 2.11.2025 10:21:29.
This article is licensed under a Creative Commons Attribution-NonCommercial 3.0 Unported Licence.

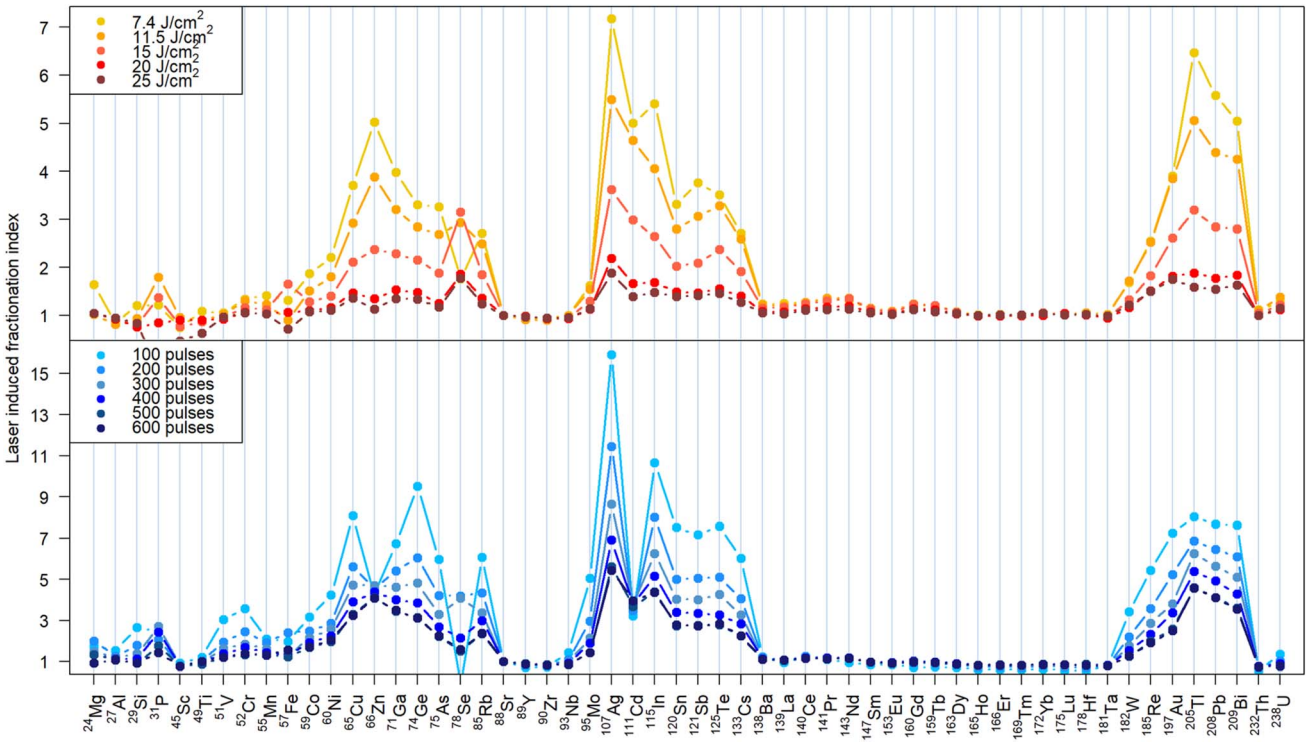

Fig. 6 Laser-induced fractionation indices normalized to ^{88}Sr for craters generated with different fluences and 600 pulses (top) and with 7.4 J cm^{-2} and an increasing number of pulses (bottom).

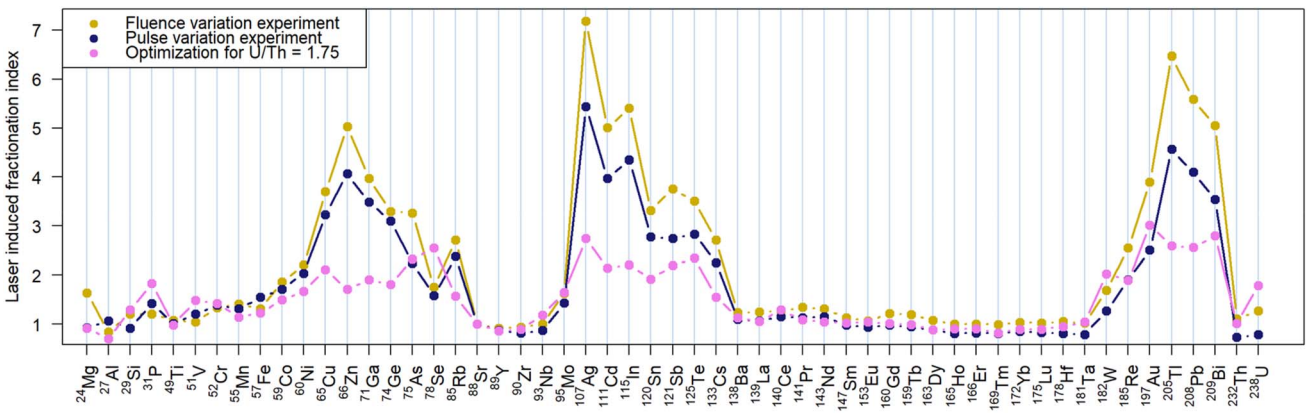

Fig. 7 Comparison of the laser-induced fractionation indices normalized to ^{88}Sr after optimization for $^{238}U^+/^{232}Th^+$ signal intensity ratios near 1 (depth and fluence) or 1.75.

volatile elements when higher laser fluences were applied. Both experiments led to lower LIFI values as the crater aspect ratio increased, but at this stage, it is not clear as to how much this is affected by the laser fluence alone and will be a topic of further investigations.

At first glance, it can be surprising that more volatile elements were enriched in the deposits and that their LIFI decreased with increasing crater aspect ratios. This is because their condensation is expected to occur at a later stage than that for the refractory elements, and they would thus get more diluted in the expanding plasma plume. However, Eggins *et al.*[7] have already proposed that vapor deposition is responsible for the enrichment of more volatile elements in the vicinity of the ablation crater, as observed here.

Impact of ICP operating conditions on elemental fractionation

To investigate the extent of the dependence of elemental fractionation on vaporization, atomization and ionization processes that occur inside the ICP, a similar experiment was carried out by adjusting the He carrier gas flow and sampling depth of the ICP to maximize the sensitivity for uranium only.

Open Access Article. Published on 20 júní 2025. Downloaded on 2.11.2025 10:21:29.
This article is licensed under a Creative Commons Attribution-NonCommercial 3.0 Unported Licence.

This resulted in a $^{238}U^+/^{232}Th^+$ signal intensity ratio of 1.75. The LIFI obtained for the different elements after the ablation experiment using 7.4 J cm^{-2} and by applying 600 laser pulses are presented in Fig. 7. A comparison with the previous values obtained after optimization for a $^{238}U^+/^{232}Th^+$ signal intensity ratio near 1 revealed a very similar pattern, yet the deviation from 1 was smaller for the more volatile elements in this experiment.

Evaluation of laser-induced fractionation is, therefore, only possible when the ICP-induced fractionation is minimized and not masking the laser-induced fractionation. In our experiments, based on the composition measured during single spot and deposit ablation, we found that laser- and ICP-induced elemental fractionation have opposite effects. The $^{238}U^+/^{232}Th^+$ signal intensity ratio of 1.75 instead of near 1 was caused by the ICP because the aerosol from single spot analysis is depleted in uranium, as indicated by the deposit analysis. By definition, the LIFI is independent of ICPMS parameters. However, the distinct variation in their values may be linked to the optimization of ICP and related processes therein. Therefore, further investigations are needed to better understand ICP-induced effects on laser aerosols.

Conclusion

Elemental fractionation in LA-ICPMS, as reported previously,[16] is considered a result of two distinct processes: one occurring at the ablation site (laser-induced) and the other within the ICPMS (ICP-induced). Analyses of single spots and the deposits remaining near the crater were carried out using the same ICPMS operating conditions. This approach enabled to establish a mass balance for the aerosol transported during crater formation and the material deposited on the sample surface, based on which the absolute transport efficiencies could be calculated. They were the lowest for volatile elements but higher than 85% for all evaluated elements.

A mathematical approach to assess inter-elemental variations caused by the laser ablation process is proposed using a mass balance approach for samples with known concentrations. This method can describe the laser-induced fractionation and is independent of isotope-specific sensitivities of the ICPMS instrument used. The LIFI of the deposits obtained using this method, in fact, closely resemble the element-specific pattern reported by Fryer based on arbitrarily selected periods of the transient signal alone.[4] However, the numeric values obtained by Fryer and the LIFI determined in our study cannot be compared because of the different experimental approaches and instrumentation.

Higher energy densities led to increased material deposition, whose chemical composition was closer to that of the bulk sample, which indicates that the extent of deposition is not directly related to the magnitude of laser-induced fractionation.

Our findings confirm that the aerosol is not only affected by laser-induced fractionation but also fractionates within the ICP. While the effects related to the ablation process highlight the intrinsic nature of the fractionation process linked to laser-matter interaction, ICP-induced fractionation can be minimized by adjusting the ICPMS operating conditions for a $^{238}U^+/^{232}Th^+$ sensitivity ratio of one. The lack of such an optimization target can lead to significant fractionation in the ICP. However, the effects of ICP-induced fractionation are currently not well comprehended and detailed studies must be carried out.

Data availability

The data supporting this article have been included as part of the ESI.†

Conflicts of interest

The authors have no conflict of interest to declare.

Acknowledgements

The financial support of Radom™ Instruments LLC. is gratefully acknowledged, and T. V. A. thanks the Research Foundation Flanders for the postdoctoral research fellowship (1218423N).

References

1 A. L. Gray, *Analyst*, 1985, **110**, 551–556.
2 S. E. Jackson, H. P. Longerich, G. R. Dunning and B. J. Fryer, *Can. Mineral.*, 1992, **30**, 1049–1064.
3 T. Hirata and R. W. Nesbitt, *Geochim. Cosmochim. Acta*, 1995, **59**, 2491–2500.
4 B. J. Fryer, S. E. Jackson and H. P. Longerich, *Can. Mineral.*, 1995, **33**, 303–312.
5 M. Shaheen, J. E. Gagnon, Z. Yang and B. J. Fryer, *J. Anal. At. Spectrom.*, 2008, **23**, 1610–1621.
6 D. Günther, R. Frischknecht, C. A. Heinrich and H.-J. Kahlert, *J. Anal. At. Spectrom.*, 1997, **12**, 939–944.
7 S. M. Eggins, L. P. J. Kinsley and J. M. G. Shelley, *Appl. Surf. Sci.*, 1998, **127–129**, 278–286.
8 R. E. Russo, X. Mao, J. J. Gonzalez and S. S. Mao, *J. Anal. At. Spectrom.*, 2002, **17**, 1072–1075.
9 A. J. G. Mank and P. R. D. Mason, *J. Anal. At. Spectrom.*, 1999, **14**, 1143–1153.
10 B. Hattendorf, C. Latkoczy and D. Günther, *Anal. Chem.*, 2003, **75**(15), 341A–347A.
11 M. Guillong and D. Günther, *J. Anal. At. Spectrom.*, 2002, **17**, 831–837.
12 D. B. Aeschliman, S. J. Bajic, D. P. Baldwin and R. S. Houk, *J. Anal. At. Spectrom.*, 2003, **18**, 1008–1014.
13 H. R. Kuhn, M. Guillong and D. Günther, *Anal. Bioanal. Chem.*, 2004, **378**, 1069–1074.
14 H. R. Kuhn and D. Gunther, *J. Anal. At. Spectrom.*, 2004, **19**, 1158–1164.
15 J. Košler, *Proc. Geol. Assoc.*, 2007, **118**, 19–24.
16 J. Košler, M. Wiedenbeck, R. Wirth, J. Hovorka, P. Sylvester and J. Míková, *J. Anal. At. Spectrom.*, 2005, **20**, 402–409.
17 B. K. Kuhn, K. Birbaum, Y. Luo and D. Günther, *J. Anal. At. Spectrom.*, 2010, **25**, 21–27.

 This journal is © The Royal Society of Chemistry 2025

Open Access Article. Published on 20 júní 2025. Downloaded on 2.11.2025 10:21:29.
This article is licensed under a Creative Commons Attribution-NonCommercial 3.0 Unported Licence.

18 J. Koch, A. Von Bohlen, R. Hergenröder and K. Niemax, *J. Anal. At. Spectrom.*, 2004, **19**, 267–272.
19 P. Becker and D. Günther, *J. Anal. At. Spectrom.*, 2023, **38**, 1704–1712.
20 H. A. O. Wang, D. Grolimund, C. Giesen, C. N. Borca, J. R. H. Shaw-Stewart, B. Bodenmiller and D. Günther, *Anal. Chem.*, 2013, **85**, 10107–10116.
21 GeoReM, Database on geochemical, environmental and biological reference materials, **http://georem.mpch-mainz.gwdg.de/**, accessed February 28, 2024.
22 K. P. Jochum, U. Nohl, K. Herwig, E. Lammel, B. Stoll and A. W. Hofmann, *Geostand. Geoanal. Res.*, 2005, **29**, 333–338.
23 R Core Team, R Foundation for Statistical Computing, Vienna, Austria, 2021.
24 RStudio Team, RStudio, PBC, Boston MA, USA, 2024.
25 R. Kovacs and D. Günther, *J. Anal. At. Spectrom.*, 2008, **23**, 1247–1252.
26 C. C. Garcia, H. Lindner and K. Niemax, *Spectrochim. Acta, Part B*, 2007, **62**, 13–19.
27 R. S. Houk, *Anal. Chem.*, 1986, **58**, 97A–105A.
28 G. R. Gillson, D. J. Douglas, J. E. Fulford, K. W. Halligan and S. D. Tanner, *Anal. Chem.*, 1988, **60**, 1472–1474.
29 K. Lodders, *Astrophys. J.*, 2003, **591**, 1220–1247.
30 *CRC Handbook of Chemistry and Physics* (Internet Version), ed. J. R. Rumble, CRC Press/Taylor & Francis, Boca Raton FL, 104th edn, 2023.